

THE UNIVERSITY OF NOTTINGHAM  
SIR PETER MANSFIELD IMAGING CENTRE  
SCHOOL OF PHYSICS AND ASTRONOMY

---

**Developing Techniques for Quantitative Renal Magnetic  
Resonance Imaging**

---

*Author:* Alexander James DANIEL MSci      *Supervisor:* Prof. Susan FRANCIS

5<sup>th</sup> March, 2021



Thesis submitted to the University of Nottingham for the degree of Doctor of Philosophy

It's very hard to talk quantum using a language originally designed to tell other monkeys where the ripe fruit is.

---

Terry Pratchett, *Night Watch*

## **Abstract**

Science will happen, but this bit can be read by muggles on ‘tinterweb.

# Contents

<b>Abstract</b>	ii
<b>Contents</b>	iii
<b>Acknowledgments</b>	viii
<b>Abbreviations</b>	ix
<b>1 Introduction</b>	1
1.1 Imaging in the Clinic . . . . .	1
1.2 Clinical Motivation . . . . .	2
1.3 Thesis Overview . . . . .	6
1.4 References . . . . .	8
<b>2 Principles of Nuclear Magnetic Resonance Imaging</b>	11
2.1 Source of the NMR Signal . . . . .	13
2.1.1 Nuclear Spin . . . . .	13
2.1.2 Application of an External Magnetic Field . . . . .	14
2.1.3 Precession . . . . .	15
2.1.4 Resonance . . . . .	16
2.2 Relaxation and Contrast Mechanisms . . . . .	18
2.2.1 Longitudinal Relaxation ( $T_1$ ) . . . . .	18
2.2.2 Transverse Relaxation ( $T_2$ and $T_2^*$ ) . . . . .	20
2.2.3 Dipole-Dipole Interactions . . . . .	25
2.2.4 Diffusion Imaging . . . . .	27
2.2.5 Optimisation of Tissue Contrast . . . . .	29

2.3	Forming an Image . . . . .	31
2.3.1	Signal Localisation . . . . .	31
2.3.2	Image Acquisition Acceleration . . . . .	38
2.3.3	Image Acquisition Schemes . . . . .	40
2.4	Conclusion . . . . .	46
2.5	References . . . . .	47
<b>3</b>	<b>Assessment of Renal <math>T_2</math> Mapping Methods</b>	<b>48</b>
3.1	Introduction . . . . .	50
3.2	Methods . . . . .	52
3.2.1	Data Acquisition . . . . .	52
3.2.2	Post Processing . . . . .	59
3.2.3	Assessment of Data . . . . .	60
3.3	Results . . . . .	66
3.3.1	Fitting Methods . . . . .	66
3.3.2	Phantom Verification . . . . .	68
3.3.3	In-Vivo . . . . .	73
3.4	Discussion . . . . .	77
3.5	Conclusion . . . . .	82
3.6	Acknowledgements . . . . .	82
3.7	References . . . . .	83
<b>4</b>	<b>Quantitative Methods to Measure Renal Oxygenation</b>	<b>89</b>
4.1	Introduction . . . . .	91
4.2	Methods . . . . .	94
4.2.1	Susceptibility-Based Oximetry . . . . .	94
4.2.2	$T_2$ Relaxation Under Spin Tagging . . . . .	96
4.2.3	Inducing Changes in Oxygenation of Blood in the Renal Vein . . . . .	102
4.3	Results and Discussion . . . . .	104
4.3.1	Susceptibility-Based Oximetry . . . . .	104
4.3.2	$T_2$ Relaxation Under Spin Tagging . . . . .	106
4.4	Conclusions and Future Work . . . . .	114

4.5	Acknowledgements . . . . .	114
4.6	References . . . . .	115
<b>5</b>	<b>Automated Segmentation of Kidneys using Machine Learning</b>	<b>120</b>
5.1	Introduction . . . . .	122
5.2	Neural Networks for Image Segmentation . . . . .	125
5.2.1	Artificial Neural Networks . . . . .	125
5.2.2	Convolutional Neural Networks . . . . .	128
5.3	Methods . . . . .	131
5.3.1	MRI Data Acquisition . . . . .	131
5.3.2	Manual Segmentation . . . . .	132
5.3.3	Automated Segmentation Using a CNN Architecture .	132
5.3.4	Statistical Analysis . . . . .	135
5.4	Results . . . . .	137
5.4.1	Characteristics of the Training Cohort . . . . .	137
5.4.2	Reducing Acquisition Time . . . . .	138
5.4.3	Accuracy of Manual Segmentation . . . . .	139
5.4.4	Network Testing . . . . .	142
5.5	Discussion . . . . .	149
5.5.1	Evaluation of Methodology . . . . .	150
5.5.2	Future Directions . . . . .	152
5.6	Conclusions . . . . .	155
5.7	Acknowledgements . . . . .	155
5.8	References . . . . .	156
<b>6</b>	<b>Ex-Vivo Renal MRI</b>	<b>162</b>
6.1	Introduction . . . . .	163
6.1.1	Validation of Multiparametric MRI via a Nephrectomy Model . . . . .	163
6.1.2	Assessment of Allograft Viability . . . . .	166
6.1.3	Ex-Vivo Protocol Aims . . . . .	166
6.2	MRI Protocol Development . . . . .	167
6.2.1	Anatomical Scans . . . . .	168

6.2.2	$T_1$ Mapping . . . . .	169
6.2.3	$T_2$ Mapping . . . . .	171
6.2.4	$T_2^*$ Mapping . . . . .	173
6.2.5	Apparent Diffusion Coefficient Mapping . . . . .	176
6.2.6	Diffusion Tensor Imaging . . . . .	180
6.3	Optimising Tissue Fixation . . . . .	189
6.4	Layer Based Analysis of Renal Data . . . . .	192
6.5	Correlating MRI Measures with Histopathology in Aged Kidneys . . . . .	192
6.6	Conclusion . . . . .	194
6.7	Acknowledgements . . . . .	194
6.8	References . . . . .	195
<b>7</b>	<b>Conclusion</b>	<b>201</b>
<b>A</b>	<b>Tractography Pipeline</b>	<b>202</b>

# **Todo list**

■ Make sure these are in the correct order . . . . .	6
■ Due to stimulate echoes? . . . . .	57
■ Would a 2D example of applying a Gaussian blur to an image be helpful here too? . . . . .	63
Figure: Individual b-values . . . . .	179

# **Chapter 6**

## **Ex-Vivo Renal MRI**

### **Abstract**

This work was presented as a digital poster at the International Society of Magnetic Resonance in Medicine (ISMRM) 27th Annual Meeting 2019 [1] and as a poster at United Kingdom Kidney Week (UKKW) 2019 [2].

## 6.1 Introduction

A recurring theme in renal Magnetic Resonance Imaging (MRI) studies are the limitations imposed by respiratory motion. Sequences must either be optimised and accelerated to fit within a breath-hold, be hugely slowed down through the use of respiratory triggering or accept the motion artefacts that are inevitable during free-breathing acquisition. Additionally the common trade-off in MRI between voxel size, Field Of View (FOV) and acquisition time becomes all the more limiting within the constraints of respirator motion. While these issues are ever-present in day-to-day clinical practice, they also impeded progress, and ultimately, clinical adoption, of techniques in the research phases of their development. Often in research, it is desirable to acquire data of higher quality than would be required in clinical practice. This can be to gain a better understanding of the spacial variance within small structures or acquire best case scenario data with many averages/time points to compare to existing, non-imaging, diagnostic techniques.

In this chapter, techniques for ex-vivo renal MRI are developed. These allow research to be conducted without the limitations imposed by respiratory motion and, in future, could be used in the clinic to assess allograft viability prior to transplant.

### 6.1.1 Validation of Multiparametric MRI via a Nephrectomy Model

Blood and urine tests are commonly used to assess renal health and function however, these are indirect measures and give no indication as to the health of individual kidneys. Consequently, the gold standard in renal diagnostics is a biopsy followed by histological analysis. During a renal biopsy, an area on the patient's back is injected with local anaesthetic then, using ultrasound as a guide, a biopsy needle is inserted into the kidney to remove a

## 6.1. Introduction

---

sample of the tissue. Acquiring the biopsy takes approximately half an hour. The patient is then asked to lie in bed for several hours to minimise the risk of internal bleeding. In approximately 1% of patients, the bleeding caused will require a blood transfusion and approximately 0.5% of patients will require embolisation. While these risks are relatively small, the procedure is still an invasive, destructive and time consuming one for the patient thus making it poorly suited for longitudinal monitoring of renal health. Additionally, this method of biopsy is not viable for some patients such as those with coagulopathy or thrombocytopenia due to the increased risk if a hemorrhage occurs or those that are unable to lie prone such as patients who are intubated for respiratory assistance [3]. While techniques such as the transjugular renal biopsy have been developed (albeit accidentally after taking a wrong turn at the portal vein while trying to acquire a liver biopsy [4]) to serve these patients, this is a more technically complicated procedure. Finally, the samples acquired via biopsy are very small and thus are often not representative of the entirety of the kidney biopsied, let alone both kidneys.

These drawbacks have provided the incentive for the development of multiparametric renal MRI protocols which could prove to be advantageous for both clinicians and patients. A key aspect in the widespread adoption of MRI into renal clinical practice, is a full understanding of the interplay between the current histological pipelines and the newly developed MRI measurements. While it is possible to correlate biopsy results with MRI findings and gain some information as to how different MRI measurements vary with tissue properties, this paradigm still suffers from the small tissue sampling volumes outlined above and the inherent difficulties of in-vivo MRI data acquisition [5]. An alternative paradigm is to scan the kidney in-vivo to collect typical renal MRI data, scan the organ ex-vivo to acquire exquisite MRI data of a far higher quality than would be possible in-vivo, then perform whole organ histology on the tissue. These three streams of complimentary data, all acquired from the same organ, eliminate the large issues with currently implemented paradigms, while still being able to reference the data back to clinically feasible measures.

## 6.1. Introduction

---

One of the first works correlating multiparametric MRI with renal histology was by Inoue *et al*, who found a statistically significant correlation between fibrosis area, as determined from a renal biopsy stained with Masson's trichrome, and Apparent Diffusion Coefficient (ADC) and  $T_2^*$  in 37 Chronic Kidney Disease (CKD) patients [6]. This was confirmed by Zhao *et al*, who found a strong correlation between ADC of both the renal cortex and medulla and histopathological fibrosis score on 25 more CKD patients [7]; this study used a more comprehensive histopathology protocol. Feng *et al* also found a correlation between glomerulosclerosis, fibrosis, Fractional Anisotropy (FA) and ADC in CKD subjects [8]. Friedli *et al* found a significant correlation between cortical-medullary differences in  $T_1$  and ADC and fibrosis, this was first found in rats, including histology of whole organs rather than just biopsy samples [9]. The same group then validated this finding in 164 human subjects, correlating with biopsy rather than whole organ [10].

Outside the renal community, work has been done with registered whole-mount histology and both in-vivo and ex-vivo MRI. Jafari *et al* have performed volume matched ex-vivo Quantitative Susceptibility Mapping (QSM) and  $T_2^*$  mapping with whole explant histopathology using the histopathology results to validate predictions of fibrosis using MRI [11]. The University of British Columbia group have carried out extensive work correlating histopathology of whole prostatectomy samples with in-vivo MRI [12, 13]. The same group have also made use of ex-vivo scanning techniques to correlate histopathology with 3T in-vivo data and 7T narrow-bore ex-vivo data [14]. The use of matched histology and MRI data is well established in the neuroimaging field [15] with studies correlating histopathology with diffusion measures [16–19], magnetisation transfer [20, 21], QSM [22, 23] and relaxometry measures [24, 25]. Additionally, post processing packages have been developed to enable accurate registration of whole mount histopathology and MRI data [26, 27].

Thus far, no work has been found comparing whole organ renal histology to in-vivo and ex-vivo MRI measurements. The ideal paradigm for this work

## **6.1. Introduction**

---

is to scan patients who are undergoing a nephrectomy as part of their standard clinical care. Briefly, this method would involve scanning a subject pre-operation to acquire a multi-parametric quantitative MRI dataset. The subject will then have part of their kidney removed, cancerous tissue will be sent for standard lab tests however, non-cancerous tissue will be immersion fixed in formalin. Equivalent scans assessing the same quantitative parameters as were collected in-vivo will be repeated ex-vivo, however these scans will be at a much higher resolution. Finally, the tissue will be sliced for multi-stain histopathology. This pipeline enables the comparison of tried and tested histological staining that clinicians are used to, albeit with larger sample sizes, with in-vivo quantitative MRI data; ex-vivo data acts as an intermediary between histology and in-vivo MRI data.

Given the purpose of this paradigm is to compare pre-existing histological analysis with newly developed, but previously documented renal MRI protocols, the area that will need the most development is the use of ex-vivo MRI to image renal tissue.

### **6.1.2 Assessment of Allograft Viability**

### **6.1.3 Ex-Vivo Protocol Aims**

To enable research into these topics, a range of ex-vivo acquisition techniques with matched in-vivo counterparts was developed with the following aims.

- Can be run on widely available hospital hardware
- Not take forever
- Not need custom coils etc
- Not time dependent i.e. can scan at any time in a 12 hour window

## 6.2 MRI Protocol Development

As one of the aims in this chapter is for the protocol developed to be able to be performed in a hospital environment, the decision to develop the protocol for use on human scanners rather than pre-clinical scanners was made. Although some hospitals are attached to research institutions with access to pre-clinical MRI scanners, this is not the norm. Imaging was performed on a 3T Philips Ingenia system as 3T scanners are available in most European/North American hospitals however some protocols were also developed for a 7T Philips Achieva system to assess the best case scenario ex-vivo images that could be acquired on human scanners, all in-vivo imaging was performed at 3T. All ex-vivo samples were scanned in 32 channel head coils, Figure 6.1, as these coils allowed for a whole organ to be imaged while also keeping array elements as close to the signal as possible. In-vivo imaging utilised a 16-channel anterior coil array and 16-channel posterior coil array.



Figure 6.1: A sample sat within the 32 channel 3T head coil.

Sequence development work was performed on formalin fixed porcine samples immersed in Phosphate-buffered Saline (PBS) at room temperature. A more detailed explanation of the sample acquisition and fixation process is provided in Section 6.3.

### 6.2.1 Anatomical Scans

To make use of the layer based analysis techniques outlined in Section 6.4 and calculate Total Kidney Volume (TKV) a high resolution, whole kidney coverage anatomical scan is required to segment the kidney from surrounding tissue/PBS. In-vivo, the  $T_2$  weighted structural scan from Chapter 5 is used. The ex-vivo protocol is outlined in Table 6.1; this scan was also used to plan subsequent ex-vivo scans.

Parameter	3T Ex-Vivo	3T In-Vivo
Voxel Size	1 x 1 x 1	1.5 x 1.5 x 5
FoV	192 x 192 x 60	350 x 350 x 71
Acquisition Mode	3D	M2D
TE	3.7	60
TR	8.1	1300
Flip Angle	15	90
Bandwidth	191.5	792.3
NSA	1	1
Fold-over Suppression Oversampling	N/A	150
Sense	2 RL, 2AP	2.5
Halfscan	0.625	N/A
Fast Imaging Mode	TFE	TSE
TFE Factor	143	N/A
Shot Interval	4000	N/A
Acquisition Time	53 sec	17 sec (1 x BH)

Table 6.1: Acquisition parameters for anatomical scans.

### 6.2.2 $T_1$ Mapping

$T_1$  mapping protocols were developed for both 3T and 7T systems using an ultrafast gradient echo inversion recovery scheme. The basics of this sequence and  $T_1$  mapping are outlined in Section 2.2.1. An example of the acquisitions at each inversion time is shown in Figure 6.2. The sequence parameters at both 3T and 7T are shown in Table 6.2.

## 6.2. MRI Protocol Development

---



Figure 6.2: Acquisitions at each of the Inversion Time (TI) at 7T.

Parameter	3T Ex-Vivo	7T Ex-Vivo	3T In-Vivo
Voxel Size	0.7 x 0.7 x 1.0	0.6 x 0.6 x 0.6	3 x 3 x 5
FoV	160 x 160 x 50	192 x 170 x 24	288 x 288 x 25
Acquisition Mode	3D	3D	MS
TE	5.1		27
TR	11		5000
TI	400, 500, 750, 900, 1100, 1300, 1500, 2000, 2600	250, 500, 750, 900, 1100, 1300, 1500, 2000, 3000	0, 100, 200, 300, 400, 500, 600, 700, 800, 900, 1000, 1100, 1300
Flip Angle	8	8	90
Bandwidth	134.4		39.3
NSA	1	2	1
Fold-over Suppression Oversampling	75	N/A	N/A
Sense	2.5 RL, 1 AP	2 RL, 1.5 AP	2.3
Halfscan	N/A	N/A	0.851
Fast Imaging Mode	TFE	TFE	EPI
TFE Factor	64	240	N/A
Shot Interval	3000	8000	N/A
Acquisition Time	1 hr 20 min 20 sec		1 min 10 sec (Trig)

Table 6.2:  $T_1$  mapping protocols and 3T and 7T.

After a  $180^\circ$  inversion, the signal sampled at each inversion time is proportional to the modulus of the true longitudinal magnetisation, as such, the true dynamic range of the inversion recovery is not sampled. This factor means there is ambiguity as to the polarity of signals near the null point (zero crossing) and can lead to a decreased accuracy when fitting for  $T_1$  as any algorithm is essentially having to fit an extra parameter in the form of the null point.

## 6.2. MRI Protocol Development

---

If the phase of the signal has been saved, the polarity of the magnitude can be corrected using the methods of Szumowski *et al* [28] thus increasing accuracy by increasing dynamic range and removing ambiguity as to the location of the null point for each voxel. Phase data is only accurate if partial Fourier acquisition acceleration techniques (Section 2.3.2), known as halfscan, are not utilised however, because these acceleration methods result in a decreased Signal to Noise Ratio (SNR) they would not be used ex-vivo anyway.

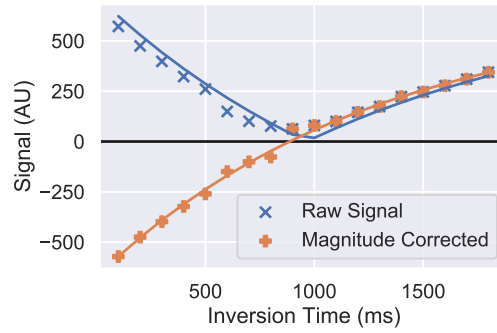


Figure 6.3: The raw signal recorded from a single voxel and the magnitude corrected signal with increased dynamic range.

Once the data has been polarity corrected, a voxel by voxel, least squares trust region reflective method is used to fit the data from each voxel to Equation (6.1) to estimate the  $T_1$  and  $M_0$  of the tissue and an uncertainty in the fit [29].

$$S(TI) = M_0 \left( 1 - 2 \cdot e^{-TI/T_1} \right) \quad (6.1)$$

Using these techniques, the  $T_1$  of ex-vivo samples could be calculated at both 3T and 7T, Figure 6.4. For in-vivo acquisitions, halfscan was used and as such magnitude correction could not be employed. As such, in-vivo data was fit to the modulus of Equation (6.1).

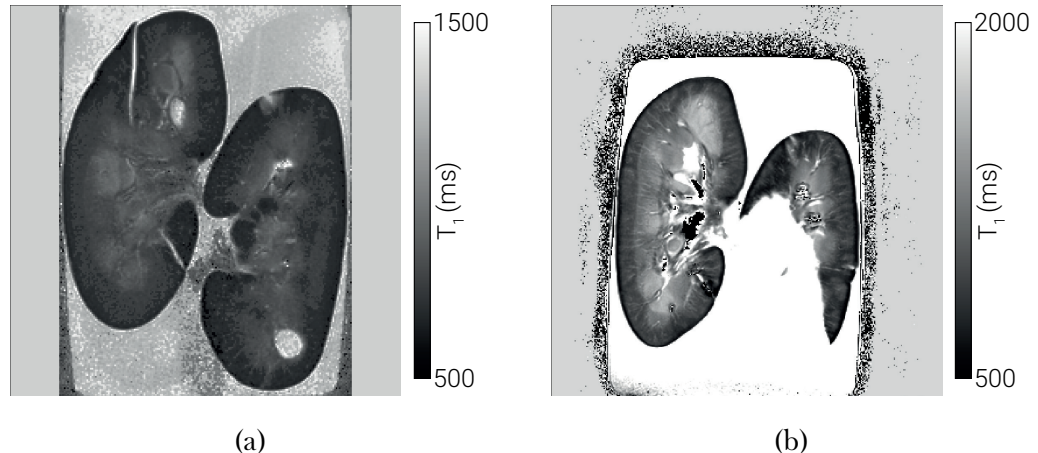


Figure 6.4: Example  $T_1$  maps generated at both 3T (a) and 7T (b).

### 6.2.3 $T_2$ Mapping

$T_2$  mapping makes use of the Gradient Spin Echo (GrASE) sequence developed in Chapter 3. This sequence was only implemented at 3T, an example of the acquisitions at each Echo Time (TE) is shown in Figure 6.5 and the sequence parameters are shown in Table 6.3. The very wide range of TE sampled ex-vivo will enable future multi-exponential analysis of the data allowing for a more accurate quantification of the long  $T_2$  components of the tissue [12, 30].

## 6.2. MRI Protocol Development

---

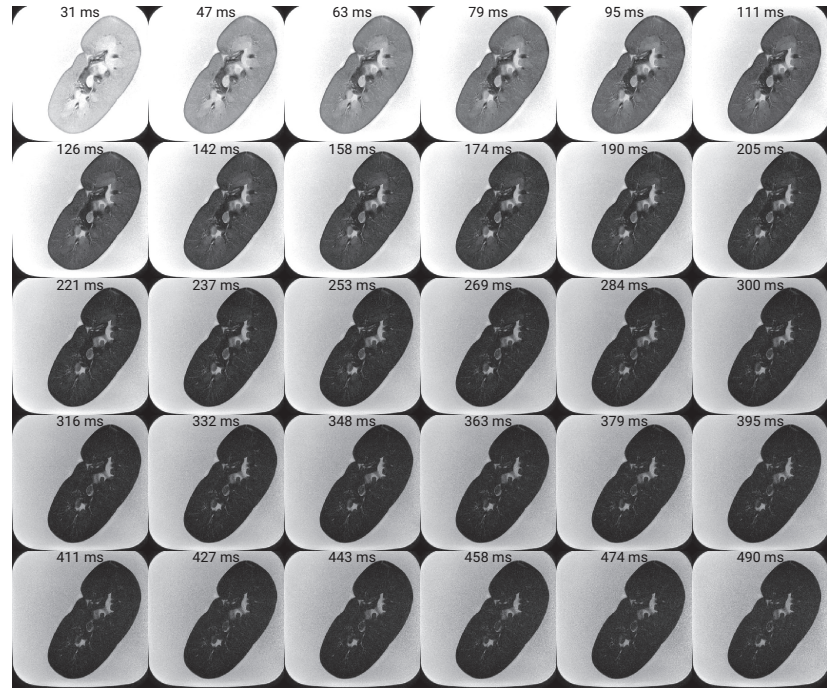


Figure 6.5: Acquisitions of an ex-vivo sample at each of the TE.

Parameter	3T Ex-Vivo	3T In-Vivo
Voxel Size	0.7 x 0.7 x 1.0	3 x 3 x 5
FoV	160 x 160 x 20	288 x 288 x 25
Acquisition Mode	MS	MS
TE	31:15.8:489.9	11:5.6:179
TR	3000	3000
Flip Angle	90	90
Bandwidth	118.9	427.9
NSA	2	1
Fold-over Suppression Oversampling	75	66
Sense	2.55	2.55
Halfscan	N/A	N/A
Fast Imaging Mode	GraSE	GraSE
TFE Factor	30	30
EPI Factor	3	3
Startup Echoes	1	1
Acquisition Time	30 min 30 sec	3 min 9 sec (Trig)

Table 6.3:  $T_2$  mapping sequence parameters.

$T_2$  maps are generated on a voxel by voxel basis using a least squares trust region reflective methods to fit the data to Equation (6.2) to estimate  $T_2$  and

$M_0$ .

$$S(TE) = M_0 \cdot e^{-TE/T_2} \quad (6.2)$$

As outlined in Section 3.3.1 multiple methods of estimating  $T_2$  were compared with the basic two parameter fit delivering the most desirable results. Using this pipeline,  $T_2$  maps could be generated, an example of which is shown in Figure 6.6. While partial voluming has been minimised by keeping voxel sizes small, the use of multi-exponential fitting models should be explored in future. This would allow the long  $T_2$  components of the signal, such as the signal from PBS to be modelled separately to the renal tissue, thus increasing accuracy.

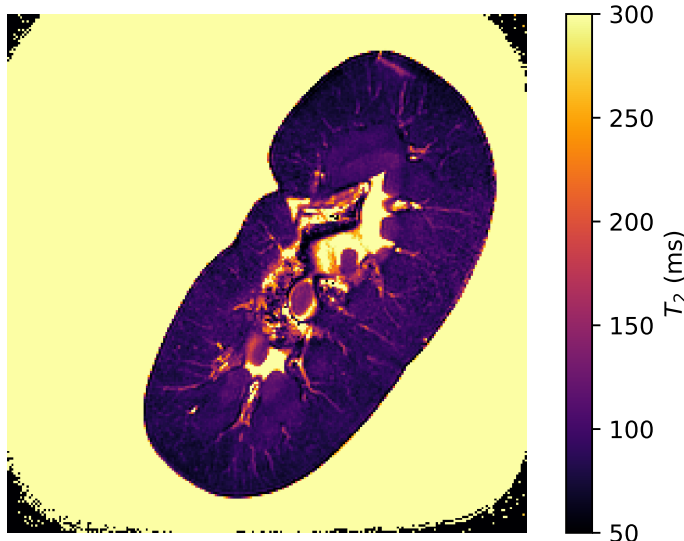


Figure 6.6: An example ex-vivo  $T_2$  map acquired using the scheme above. This sample had been formalin fixed and stored in PBS for multiple months, hence the lack of contrast between cortical and medullary tissue.

### 6.2.4 $T_2^*$ Mapping

$T_2^*$  acquisition is performed using a simple multi-slice gradient echo sequence as outlined in Section 2.2.2 and was developed at both 3T and 7T. The acquisition parameters are shown in Table 6.4. In addition to the magnitude data saved for  $T_2^*$  mapping, the phase data is also saved to allow a QSM

## 6.2. MRI Protocol Development

---

pipeline to be developed in future.

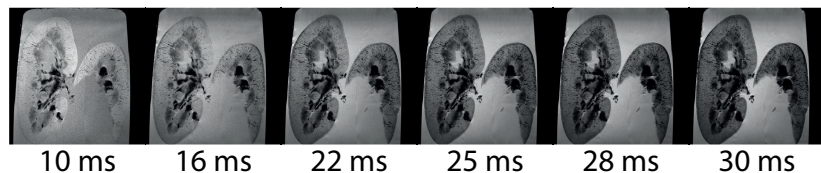


Figure 6.7: Acquisitions at each of the TE at 7T.

Parameter	3T Ex-Vivo	7T Ex-Vivo	3T In-Vivo
Voxel Size	0.7 x 0.7 x 1.0	0.5 x 0.5 x 1	1.5 x 1.5 x 5
FoV	160 x 160 x 25	145 x 145 x 10	288 x 288 x 25
Acquisition Mode	MS	MS	MS
TE	15:5:50	10, 13, 16, 19, 22, 25, 28, 30	5:3:38
TR	697		79
Flip Angle	38	38	25
Bandwidth	35 - 56		1328.6
NSA	1	3	1
Fold-over Suppression Oversampling	75	N/A	144
Sense	2	2	2
Halfscan	N/A	N/A	N/A
Fast Imaging Mode	None	None	None
Acquisition Time	46 min 25 sec		47 sec (3 x BH)

Table 6.4: Acquisition parameters for  $T_2^*$  mapping sequences at 3T and 7T.

Estimation of  $T_2^*$  can be performed via two different methods, fitting to a two parameter exponential (Equation (6.3)) or performing a weighted linear fit to the natural logarithm of the signal. The latter of these methods is far less computationally intensive and as such, runs much quicker.

$$S(TE) = M_0 \cdot e^{-TE/T_2^*} \quad (6.3)$$

The acquisition parameters of the 3T ex-vivo protocol were simulated to

## 6.2. MRI Protocol Development

---

compare the two fitting methods using Monte Carlo techniques. The linear fit produces a slightly greater Coefficient of Variation (CoV) than the exponential fit at lower  $T_2^*$ , Figure 6.8a. Additionally, the relative error, defined by Equation (6.4), has a greater magnitude below 20 ms when fitting with the linear fit than the exponential fit, Figure 6.8b. The  $T_2^*$  we expect from the kidneys at 3T is greater than 20 ms so in the interests of computational efficiency, the linear fitting method was used.

$$\text{Relative Error} = \frac{t_{2 \text{ fit}}^* - t_{2 \text{ simulated}}^*}{t_{2 \text{ simulated}}^*} \quad (6.4)$$

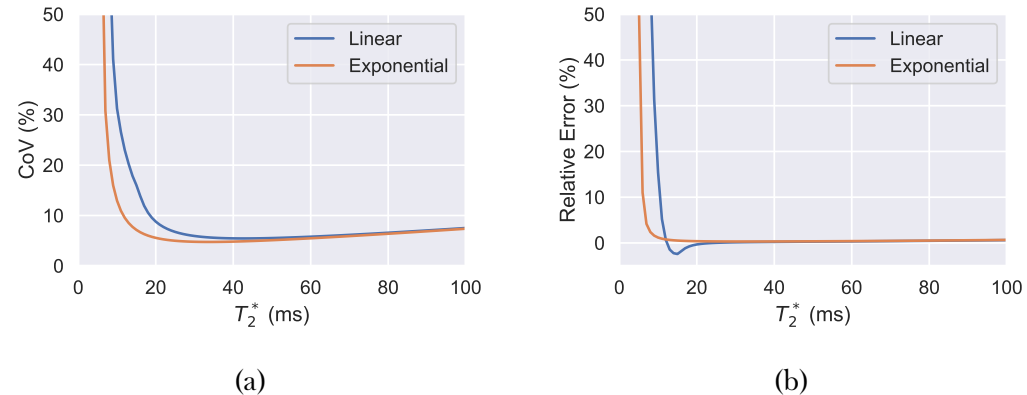


Figure 6.8: Simulations to ascertain the accuracy of each  $T_2^*$  fitting algorithm over a range of  $T_2^*$ .

Using the acquisition and post processing steps above,  $T_2^*$  maps can be generated, examples of which are shown in Figure 6.9.

## 6.2. MRI Protocol Development

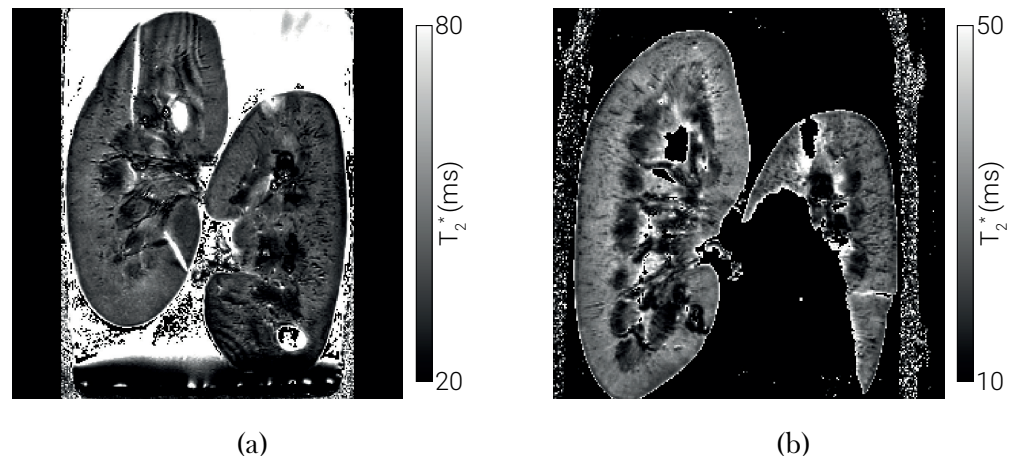


Figure 6.9: An example  $T_2^*$  map acquired at 3T (a) and 7T (b) fit using the weighted fit to the natural logarithm of the signal.

### 6.2.5 Apparent Diffusion Coefficient Mapping

The underlying principles of diffusion imaging are outlined in Section 2.2.4, here Diffusion Weighted Imaging (DWI) is performed using a single shot Spin Echo (SE)-Echo Planar Imaging (EPI) sequence over a range of b-values applied in three orthogonal directions. By acquiring diffusion gradients in three different directions and calculating the mean, the effects of diffusion anisotropy can be minimised. The sequence was developed for 3T systems with a schematic of the sequence shown in Figure 6.10 and the sequence parameters summarised in Table 6.5.

## 6.2. MRI Protocol Development

---

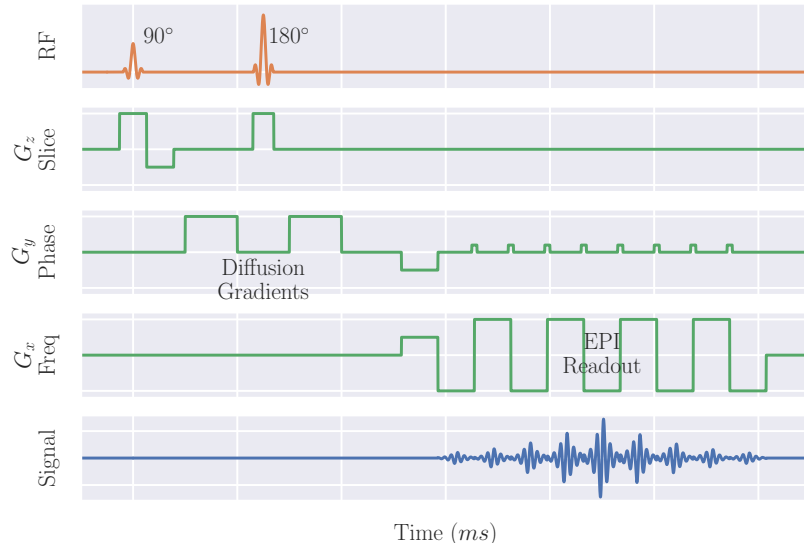


Figure 6.10: A schematic of the SE-EPI sequence used for ADC mapping. This block is repeated multiple times with diffusion gradients applied in different directions and with different strengths.

Parameter	3T Ex-Vivo	3T In-Vivo
Voxel Size	1.5 x 1.5 x 1.5	1.5 x 1.5 x 5
FoV	160 x 160 x 51	288 x 288 x 25
Acquisition Mode	MS	MS
TE	72	71
TR	1800	1800
b-values	0, 5, 15, 30, 45, 60, 75, 90, 105, 120, 135, 150, 175, 200, 300, 400, 500, 600	0, 5, 15, 30, 45, 60, 75, 90, 105, 120, 135, 150, 175, 200, 300, 400, 500, 600
Flip Angle	90	90
Bandwidth	13.2	13.7
NSA	1	1
Fold-over Suppression Oversampling	75	N/A
Sense	2.3	2.3
Halfscan	0.676	0.676
Fast Imaging Mode	EPI	EPI
EPI Factor	91	83
Phase Encode Direction	L then R	L then R
Acquisition Time	9 min 44 sec	2 min 42 sec (Trig)

Table 6.5: ADC mapping acquisition parameters.

## 6.2. MRI Protocol Development

---

The diffusion sensitising block of the pulse sequence is time consuming and as such necessitates the use of fast image techniques, EPI is the simplest to implement however is not without drawbacks. It suffers from geometric distortions, particularly in the phase encode direction, due to inhomogeneities in the  $B_0$  field cause by susceptibility differences. These geometric distortions can be problematic for this paradigm as the ability to correlate, on a voxel by voxel basis, parameters acquired with different sequences is at the core of multiparametric MRI. Geometric distortions make this impossible. The susceptibility of PBS and renal tissue is similar however there is a very large difference between the PBS and surrounding air and as such, distortions can be problematic.

As the distortions are predominantly in the phase encode direction, by inverting the direction of the phase encode blips, the direction of the distortion can be reversed, Figure 6.11a. By acquiring images with both phase encode directions the underlying field map can be estimated and used to undistort the data [31]. This process can be carried out using fMRI Software Library (FSL) “topup” however, as this tool was designed for work in the brain, a custom configuration to perform more iterations of the field estimation algorithm with a greater degree of regularisation is required.

Although in some cases it is possible to acquire only the  $b_0$  image in both phase encode directions, calculate the displacement field, then apply this field to other  $b$ -values, it was decided that the  $\sqrt{2}$  SNR increase of acquiring two volumes and averaging them is beneficial. Additionally if, in the case of in-vivo data, there are issues with motion in the  $b_0$  volumes, then another diffusion weighting can be used to estimate the displacement, thus adding inherent redundancy to the pipeline.

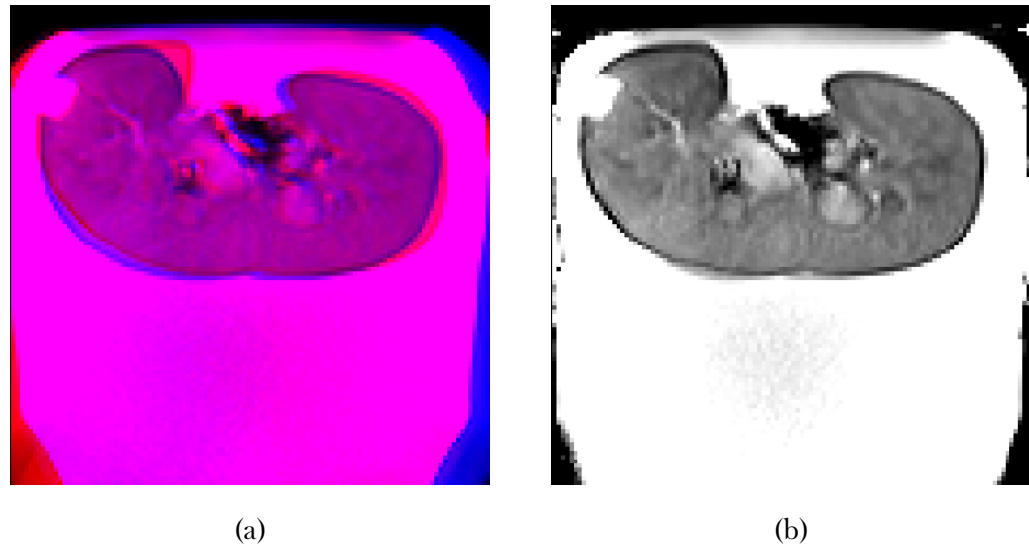


Figure 6.11: (a) b0 images collected with opposing phase encode directions overlay in red and blue. (b) A composite image with EPI distortions corrected using topup.

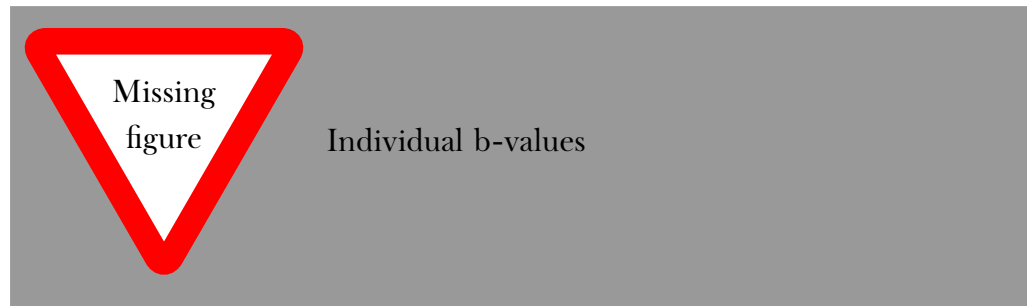


Figure 6.12: Distortion corrected images at each b-value.

The average of the three directions at each b-value and phase encode direction is calculated. EPI distortion correction is performed on both ex-vivo and in-vivo data using topup to enable accurate voxel by voxel comparison of ADC to other quantitative parameters. The natural logarithm of the distortion corrected signal from each voxel over each b-value is taken and a linear least squares fit performed. This enables a quick estimation of ADC and an uncertainty in the fit.

Using these techniques, the ADC of both in-vivo and ex-vivo renal tissue can be calculated, Figure 6.13 with no geometric distortions. Although not

## 6.2. MRI Protocol Development

---

implemented here, the large number of low b-values sampled should make estimations of more advance diffusion parameters possible such as fitting the data to an Intravoxel Incoherent Motion (IVIM) model [32].

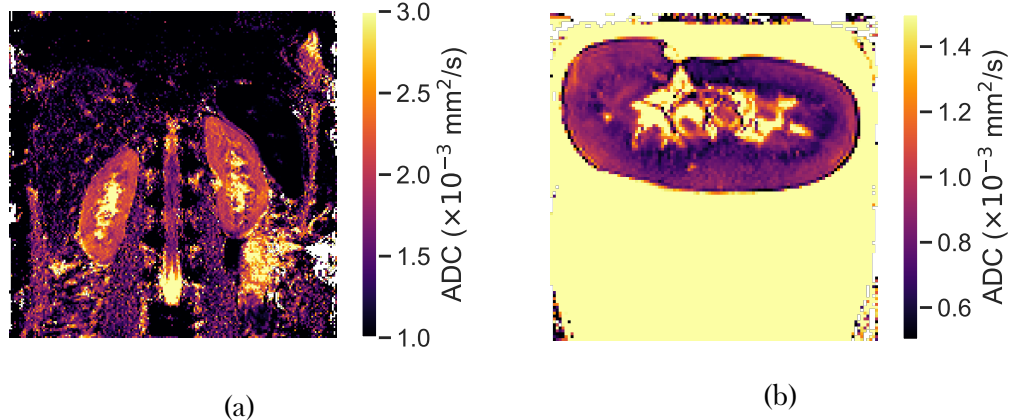


Figure 6.13: ADC maps acquired of both an in-vivo subject (a) and ex-vivo sample (b).

### 6.2.6 Diffusion Tensor Imaging

ADC maps provide an understanding as to how readily molecules can diffuse through a tissue, however they do not provide any information as to what directions the molecules are travelling, to measure this, Diffusion Tensor Imaging (DTI) is used. The renal group at Sir Peter Mansfield Imaging Centre (SPMIC) had no existing high resolution in-vivo (or ex-vivo) DTI protocol, as such this was specifically developed for this paradigm.

The acquisition scheme used is very similar to that in Section 6.2.5, a single shot SE-EPI scheme with monopolar diffusion gradients. The difference lies in the fact that, rather than acquiring a large range of b-values over three different directions, only a  $b_0$  and one other b-value are acquired over a minimum of six directions although in practice, many more. This is known as a single shell DTI scheme. As the diffusivity in, for example, the positive  $x$  direction is the same as the negative  $x$  direction most DTI schemes acquire a hemisphere of directions, however, to apply additional image deformation

## 6.2. MRI Protocol Development

---

correction techniques outlined below, diffusion vectors were acquired over a full sphere, Figure 6.14.

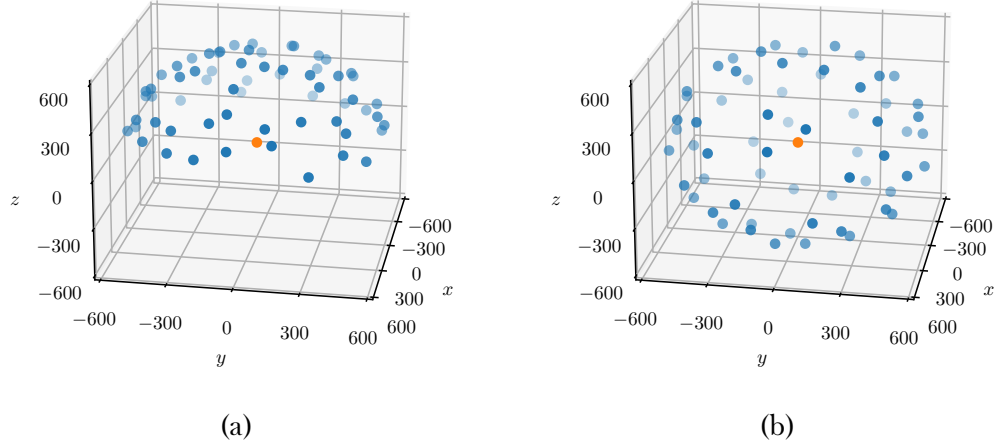


Figure 6.14: (a) 64 diffusion directions acquired over a hemisphere (b) 64 diffusion directions acquired over a full sphere as used in this chapter.  $b_0$  is shown in orange with subsequent  $b$ -values shown in blue.

Mathematically, DTI is estimating the tensor,  $\mathcal{D}$  in equation (6.5) where  $D_{xx}$ ,  $D_{yy}$  and  $D_{zz}$  represent diffusivity along the  $x$ ,  $y$  and  $z$  directions in the lab frame and are equivalent to the three directions sampled in Section 6.2.5.  $D_{yx}$ ,  $D_{zx}$  and  $D_{zy}$  represent diffusivity between the principle axis of the lab frame, as  $\mathcal{D}$  is symmetric,  $D_{yx} \equiv D_{xy}$ ,  $D_{zx} \equiv D_{xz}$  etc, hence DTI can be performed by only sampling a hemisphere of diffusion vectors.

$$\mathcal{D} = \begin{bmatrix} D_{xx} & D_{xy} & D_{xz} \\ D_{yx} & D_{yy} & D_{yz} \\ D_{zx} & D_{zy} & D_{zz} \end{bmatrix} \quad (6.5)$$

Like the ADC sequence, a full dataset is acquired with both opposing phase encode directions to assist with geometric distortion correction. A summary of the sequence parameters is shown in Table 6.6.

## 6.2. MRI Protocol Development

---

Parameter	3T Ex-Vivo	3T In-Vivo
Voxel Size	2.3 x 2.3 x 2.3	3 x 3 x 3
FoV	160 x 160 x 51	288 x 288 x 60
Acquisition Mode	MS	MS
TE	85	82
TR	5100	5100
b-values	0, 600	0, 600
Directions	128	64
Flip Angle	90	90
Bandwidth	17.1	30.5
NSA	2	1
Fold-over Suppression Oversampling	100	N/A
Sense	2	2
Halfscan	0.609	0.609
Fast Imaging Mode	EPI	EPI
EPI Factor	79	47
Phase Encode Direction	L then R	L then R
Acquisition Time	52 min 42 sec	8 min 10 sec (Trig)

Table 6.6: DTI acquisition parameters.

The large number of diffusion directions sampled makes additional geometric distortion possible. The rapidly switching fields of the diffusion sequence induce eddy currents in the sample, which in turn induce an opposing magnetic field. This leads to off-resonance distortions in the image. To combat this FSLs “eddy” can be used [33]. This tool was developed with the brain data from the Human Connectome Project in mind however [34], here it is successfully used to reduce geometric distortions in ex-vivo and in-vivo DTI data and subject motion in the in-vivo data. The tools performance is optimal when b-vectors are distributed over a full sphere as this results in approximately opposing eddy current distortions and as such, makes estimation of the deformation more accurate.

Once the raw data has been processed with topup and eddy, quantitative maps can be generated. Eigenvalues ( $\lambda_1, \lambda_2, \lambda_3$ ) and eigenvectors ( $\epsilon_1, \epsilon_2, \epsilon_3$ ) are calculated for each diffusion tensor,  $\mathcal{D}$ . FA maps can be calculated from equation (6.6). Here it can be seen that if  $\lambda_1 = \lambda_2 = \lambda_3$ , as is the case

## 6.2. MRI Protocol Development

---

for isotropic diffusion, FA tends to 0. An example renal FA map is shown in Figure 6.15a where bright areas represent areas of higher FA and therefore more anisotropic diffusion.

$$FA = \sqrt{\frac{(\lambda_1 - \lambda_2)^2 + (\lambda_2 - \lambda_3)^2 + (\lambda_1 - \lambda_3)^2}{2(\lambda_1^2 + \lambda_2^2 + \lambda_3^2)}} \quad (6.6)$$

FA can also be used to create fibre direction maps as shown in Figure 6.15b. Here the colour is determined by the direction of the principal eigenvector,  $\epsilon_1$ , the primary direction of diffusion, and the brightness is modulated by FA. As the name suggests, these maps provide a visual indication as to the direction diffusion is occurring in a tissue and how strongly it is constrained to that single direction.

The final voxel based map produced using the DTI data is an ADC map, often called Mean Diffusivity (MD) in DTI literature. This is calculated using equation (6.7) and an example is shown in Figure 6.15c. All three of these voxel based maps are generated using FSL.

$$MD = \frac{(\lambda_1 + \lambda_2 + \lambda_3)}{3} \quad (6.7)$$

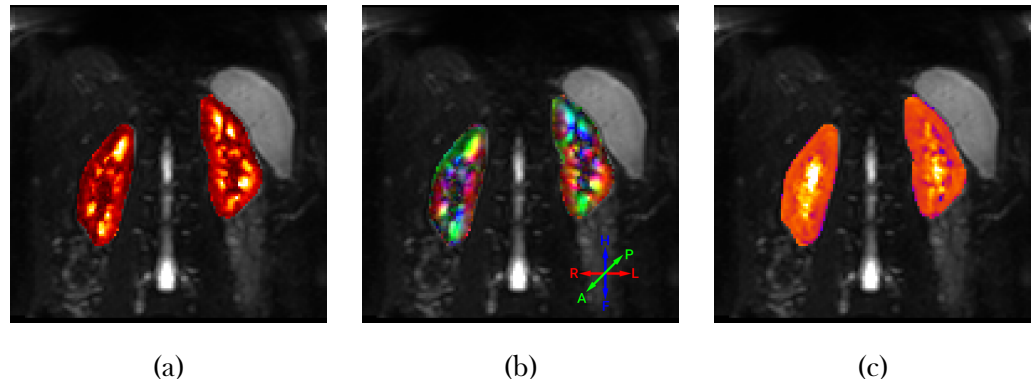


Figure 6.15: FA (a), fibre direction (b) and MD (c) maps generated from the same in-vivo DTI data.

## 6.2. MRI Protocol Development

---

An extension of the fibre direction map is tractography, a technique that can remove the simplification that a voxel has a single direction of diffusion. Even at the highest resolutions achievable with MRI, the biological structures dictating diffusion are orders of magnitude smaller than the resolving power of MRI and as such multiple mechanisms can occur in a single voxel e.g. crossing of neurons or microvascular. In the brain this technique is used to visualise nerve tracts and connectivity within the brain; in the kidneys it can be used to visualise the coherent motion of renal processes. Tractography calculations are performed using the open-source python package Dipy [35] and the resulting tracts were visualised using TrackVis [36].

To model multiple fibres entering and exiting a voxel, a more sophisticated model than simply looking at the principle eigenvector is required. This takes the form of an Orientation Distribution Function (ODF) which can be thought of as the probability a fibre will enter or exit a voxel through a specific solid angle. ODFs can be visualised as isosurfaces where the surface represent all points of equal probability, example ODFs are shown in Figure 6.16. Techniques such as Q-ball imaging [37, 38] and diffusion spectrum imaging [37] can be used to estimate the ODF however these methods tend to require high b-values and as such a lower SNR acquisition making them less suitable to abdominal imaging. Instead a constrained spherical deconvolution method is used [39–41].

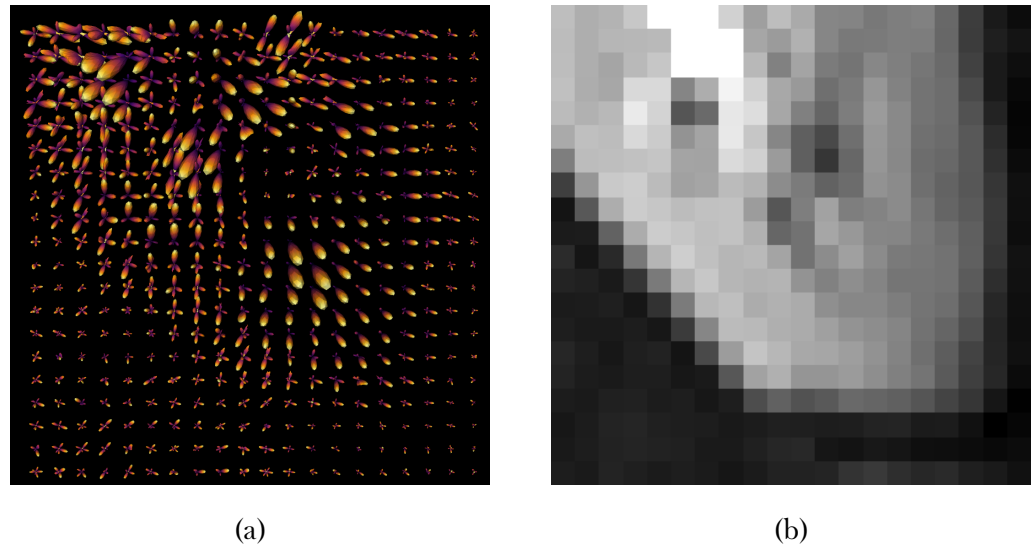


Figure 6.16: The ODFs for a small number of voxels of renal tissue (a) and the corresponding b0 image to help visualise the part of the kidney the data is coming from (b).

The peak values of ODFs are calculated and used to generate streamlines which represent the tracts of coherent diffusion. The calculation of streamline paths is performed using the Euler Delta Crossings (EuDX) method [42]. This tractography pipeline and its many hyper-parameters are best summarised in code form and as such are included in Appendix A. The results of this processing pipeline are tractograms as shown in Figure 6.17.

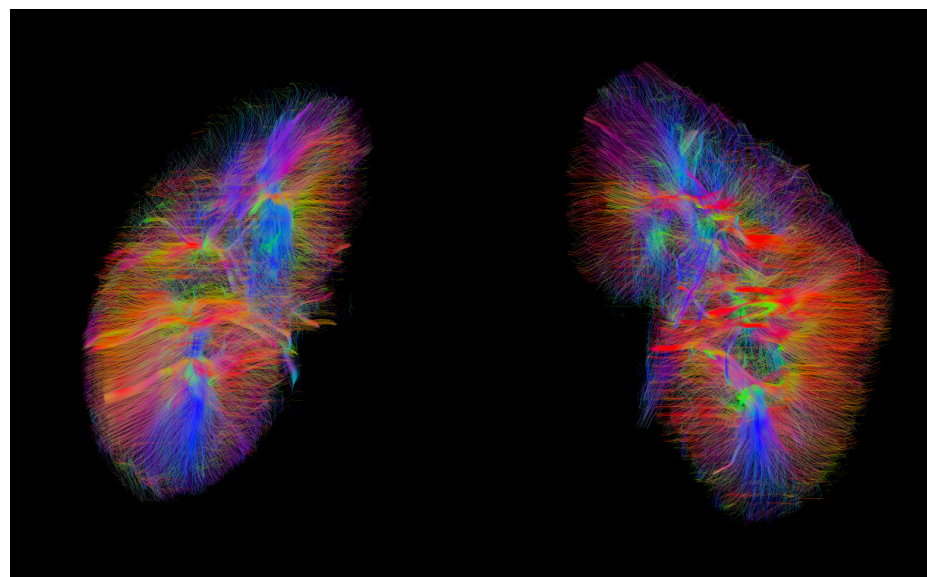


Figure 6.17: Example tractography generated using the above protocol.

## 6.2. MRI Protocol Development

---

As this tractography protocol was developed from scratch, both acquisition and the post processing pipeline were verified in the brain. Tractography is a far more mature technique in neuroimaging and as such, verification that the pipeline produces reasonable results on a more familiar anatomy lends confidence to the tractograms produced of the kidneys. The FOV of the acquisition was adjusted to cover the whole brain but all other parameters were kept constant. The resulting maps and tractogram were all as expected, an example tractogram of the brain produced using this pipeline is shown in Figure 6.18.

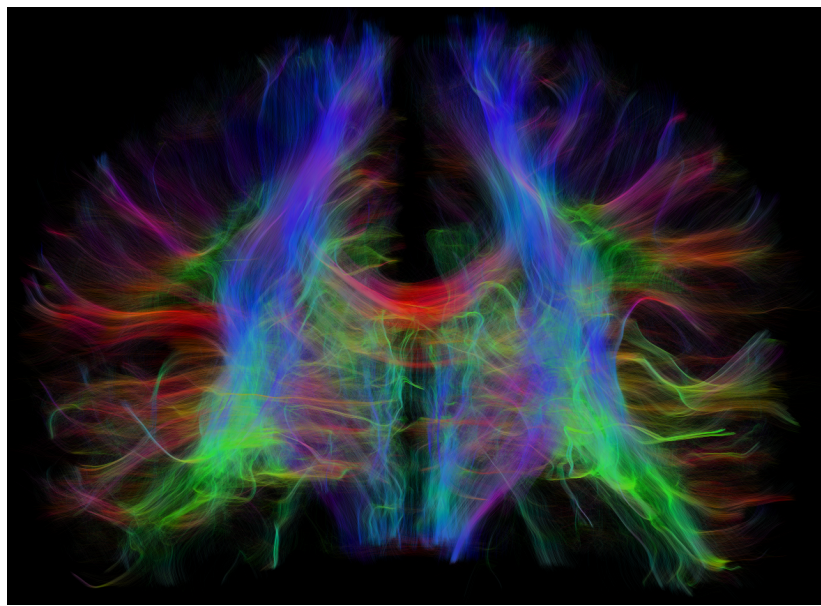


Figure 6.18: A tractogram of the brain produced to verify the DTI acquisition and post-processing scheme developed for the kidneys produces expected results within a structure more commonly the subject of tractography.

Renal in-vivo results were compared to those in literature and found to be in agreement [43–45]. Additionally, renal features with a known structure can be observed in the tractograms such as the radial structure of the medullary pyramids, Figure 6.19.

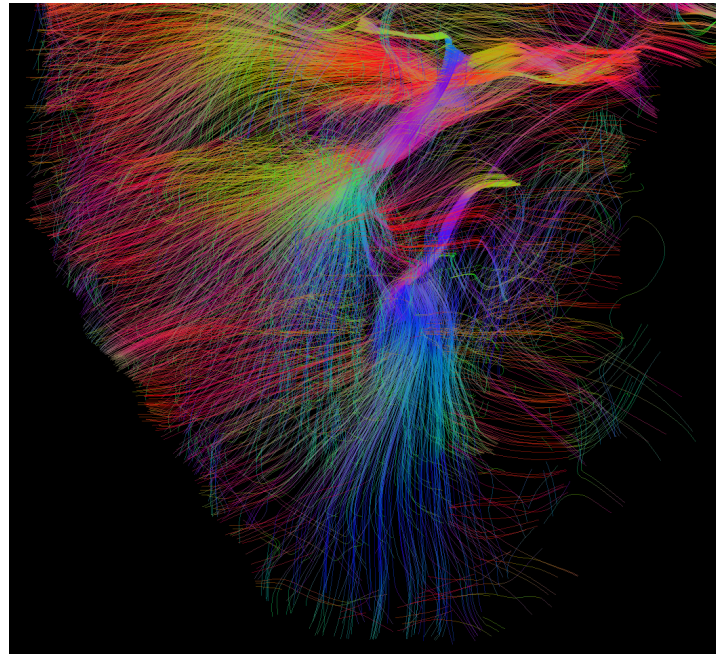


Figure 6.19: The medullary pyramids observed in tractography.

An area that still needs further development is the ex-vivo DTI protocol. There are promising early results however ex-vivo diffusion imaging poses additional difficulties. During the fixation process, methyl bridges cross link with proteins within the tissue stiffening it and causing a small amount of shrinkage [46]. This combined with the lower temperatures of ex-vivo samples ( $\sim 20^{\circ}\text{C}$  room temperature rather than  $\sim 37^{\circ}\text{C}$  body temperature) leads to a reduced degree of diffusion, seen in Figure 6.13. While this results in a higher SNR of diffusion sensitised volumes for a given b-value, the underlying diffusion signal being measured is much smaller i.e. there is less of a difference between  $b_0$  and  $b=600 \text{ sec/mm}^2$  and thus the accuracy of the quantitative maps, Figure 6.20, and tractography, Figure 6.21 is reduced.

## 6.2. MRI Protocol Development

---

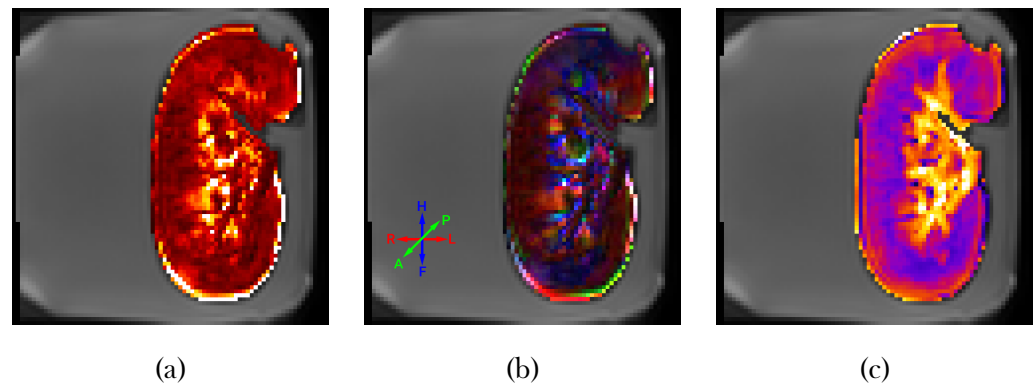


Figure 6.20: FA (a), fibre direction (b) and MD (c) maps of an ex-vivo sample.

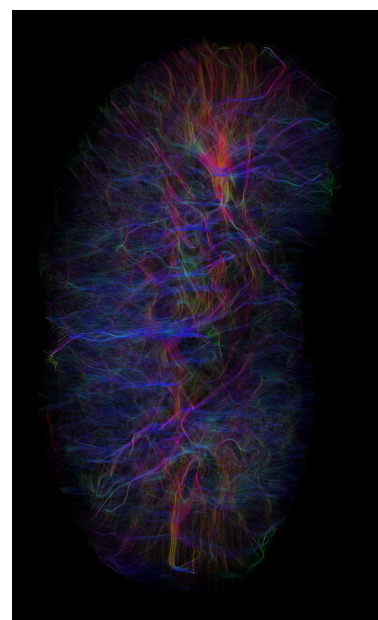


Figure 6.21: Tractography of an ex-vivo kidney sample.

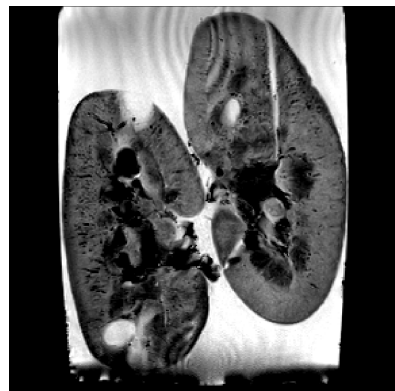
### 6.3 Optimising Tissue Fixation



(a)



(b)



(c)



(d)

Figure 6.22: (a) An example of a sample procured from the slaughterhouse after it has been fixed. The left hand kidney has been sliced in half; the right hand kidney has the incisions from the meat inspector clearly visible. (b) An example of a sample procured from Veterinary Science post fixing. (c) An example of a  $T_2$  weighted Fast Field Echo (FFE) with TE = 40 ms of a kidney procured from the slaughterhouse. (d) An example of a  $T_2$  weighted FFE with TE = 40 ms of a kidney procured from Veterinary Science.

### 6.3. Optimising Tissue Fixation

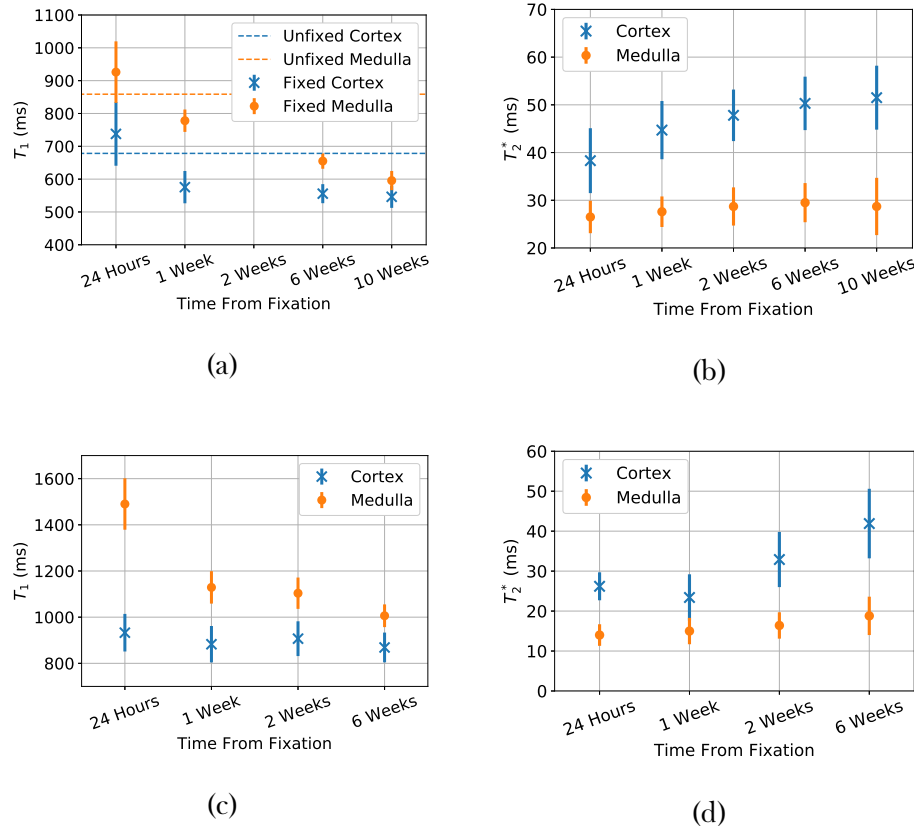


Figure 6.23: (a) Variation in  $T_1$  as a function of time after fixation measured at 3T (b) Variation in  $T_2^*$  as a function of time after fixation measured at 3T (c) Variation in  $T_1$  as a function of time after fixation measured at 7T (d) Variation in  $T_2^*$  as a function of time after fixation measured at 7T.

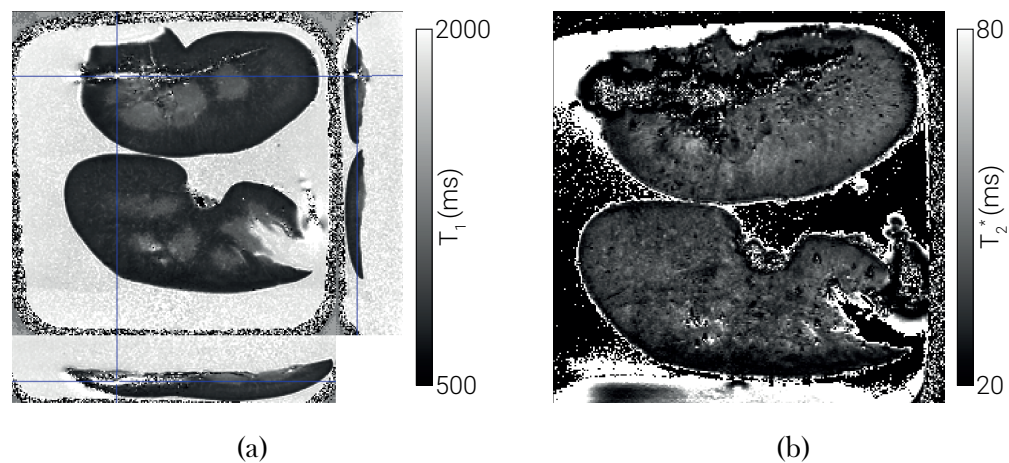


Figure 6.24: (a) An example of the  $T_1$  map collected from the short time scale kidney (b) An example of the  $T_2^*$  map collected from the short time scale kidney.

### 6.3. Optimising Tissue Fixation

---

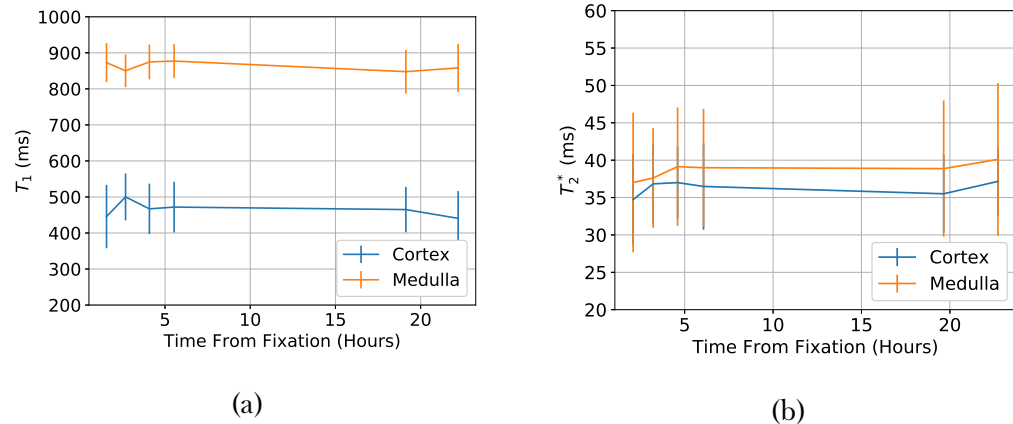


Figure 6.25: (a) Variation in  $T_1$  as a function of time after fixation measured at 3T (b) Variation in  $T_2^*$  as a function of time after fixation measured at 3T.

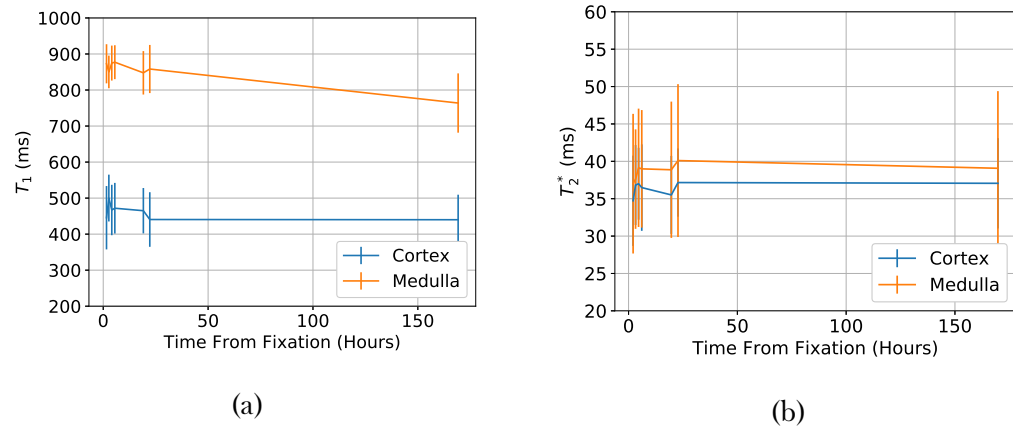


Figure 6.26: (a) Variation in  $T_1$  as a function of time after fixation measured at 3T (b) Variation in  $T_2^*$  as a function of time after fixation measured at 3T.

## 6.4 Layer Based Analysis of Renal Data

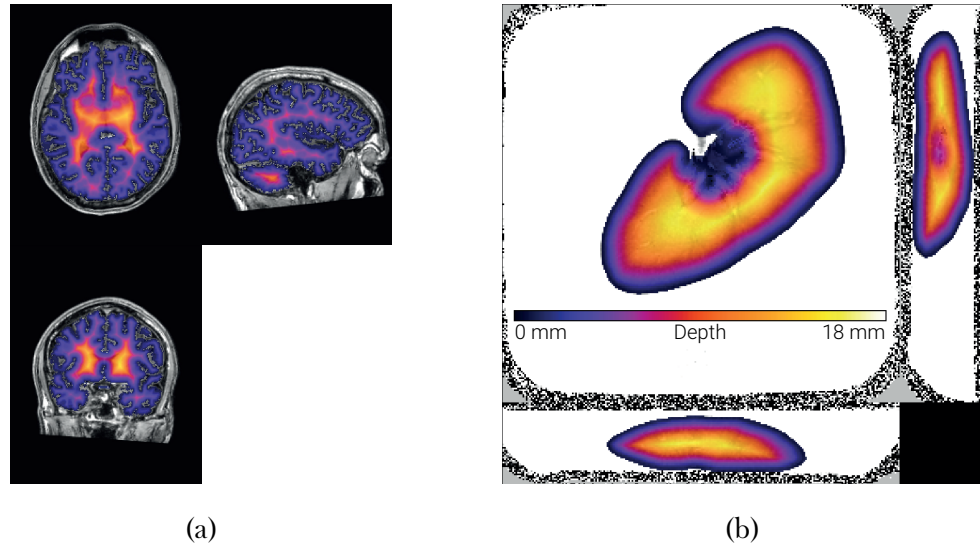


Figure 6.27: (a) A depth mask of the brain. Lighter areas are deeper inside the brain. (b) A depth mask applied to a quantitative  $T_1$  map.

## 6.5 Correlating MRI Measures with Histopathology in Aged Kidneys

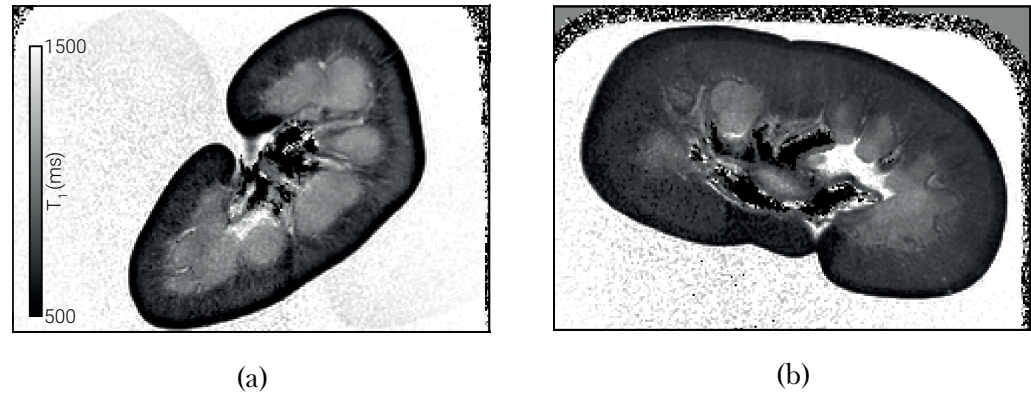


Figure 6.28: (a)  $T_1$  map of a 0.5 year old pig kidney. (b)  $T_1$  map of a 2.5 year old pg kidney.

## 6.5. Correlating MRI Measures with Histopathology in Aged Kidneys

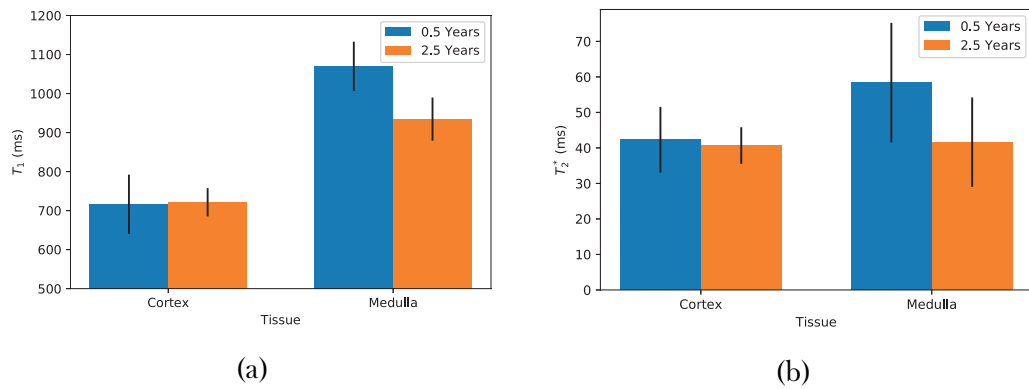


Figure 6.29: (a) The  $T_1$  of the renal cortex and medulla of the two samples.  
(b) The  $T_2^*$  of the renal cortex and medulla of the two samples.

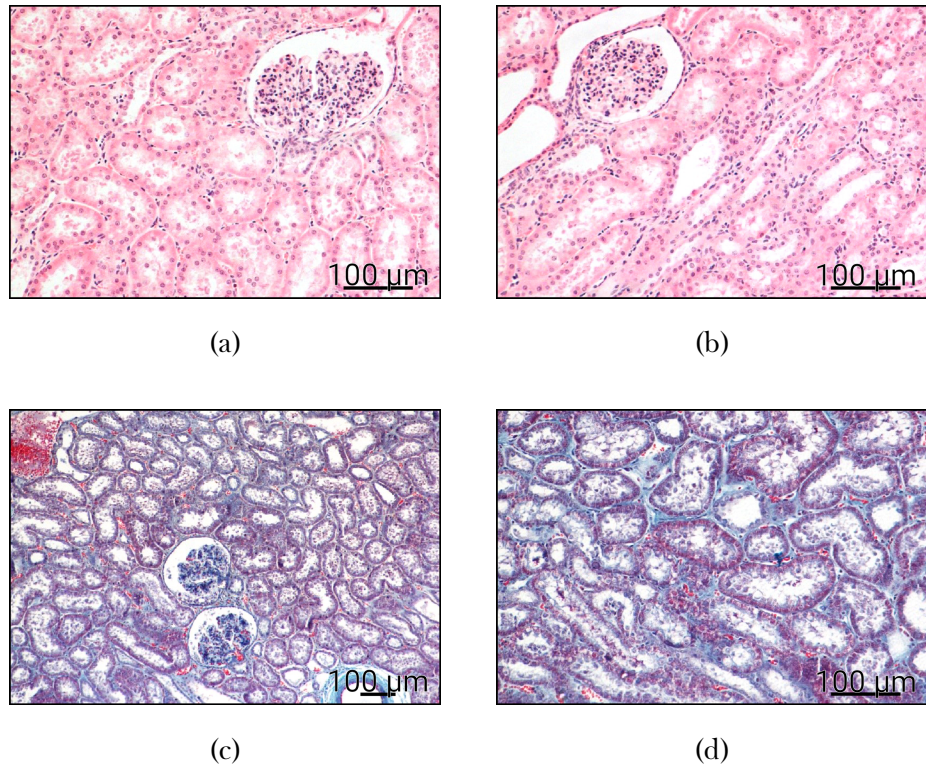


Figure 6.30: (a) A sample of renal cortex from a 0.5 year old pig stained with Haematoxylin and Eosin (H and E). (b) A sample of renal cortex from a 2.5 year old pig stained with H and E. (c) A sample of renal cortex from a 0.5 year old pig stained with Masson's trichrome. (d) A sample of renal cortex from a 2.5 year old pig stained with Masson's trichrome.

## 6.6 Conclusion

## 6.7 Acknowledgements

We are grateful for access to the University of Nottingham's Augusta high performance computing service.

## 6.8 References

1. Daniel, A. J., Buchanan, C., Kazmi, I., Cox, E., Selby, N., Gardner, D. & Francis, S. *The Effects of Fixation and Age on Relaxometry Measurements of Ex-Vivo Kidneys* in *Proc. Intl. Soc. Mag. Reson. Med.* 27 International Society of Magnetic Resonance in Medicine Annual Meeting (Montreal, 13th May 2019).
2. Kazmi, I., Daniel, A. J., Buchanan, C., Francis, S., Taal, M. & Selby, N. *Determining Optimal Technique for Tissue Fixation for Ex-Vivo MRI Imaging of Porcine Kidneys* in. United Kingdom Kidney Week (Brighton, 6th May 2019).
3. Rathod, K. R., Popat, B. A., Pandey, A., Jamale, T. E., Hase, N. K. & Deshmukh, H. L. Safety and Effectiveness of Transjugular Renal Biopsy: A Single Center Study. *Indian Journal of Nephrology* **27**, 118–123 (2017).
4. Mal, F., Meyrier, A., Callard, P., Altman, J. J., Kleinknecht, D., Beaugrand, M. & Ferrier, J. P. Transjugular Renal Biopsy. *Lancet (London, England)* **335**, 1512–1513 (23rd June 1990).
5. Leung, G., Kirpalani, A., Szeto, S. G., Deeb, M., Foltz, W., Simmons, C. A. & Yuen, D. A. Could MRI Be Used To Image Kidney Fibrosis? A Review of Recent Advances and Remaining Barriers. *Clinical Journal of the American Society of Nephrology* **12**, 1019–1028 (7th June 2017).
6. Inoue, T. *et al.* Noninvasive Evaluation of Kidney Hypoxia and Fibrosis Using Magnetic Resonance Imaging. *Journal of the American Society of Nephrology: JASN* **22**, 1429–1434 (Aug. 2011).
7. Zhao, J., Wang, Z. J., Liu, M., Zhu, J., Zhang, X., Zhang, T., Li, S. & Li, Y. Assessment of Renal Fibrosis in Chronic Kidney Disease Using Diffusion-Weighted MRI. *Clinical Radiology* **69**, 1117–1122 (Nov. 2014).
8. Feng, Q., Ma, Z., Wu, J. & Fang, W. DTI for the Assessment of Disease Stage in Patients with Glomerulonephritis - Correlation with Renal Histology. *European Radiology* **25**, 92–98 (1st Jan. 2015).

## 6.8. References

---

9. Friedli, I. *et al.* New Magnetic Resonance Imaging Index for Renal Fibrosis Assessment: A Comparison between Diffusion-Weighted Imaging and T1 Mapping with Histological Validation. *Scientific Reports* **6**. doi:10.1038/srep30088. pmid: 27439482 (21st July 2016).
10. Berchtold, L. *et al.* Validation of the Corticomedullary Difference in Magnetic Resonance Imaging-Derived Apparent Diffusion Coefficient for Kidney Fibrosis Detection: A Cross-Sectional Study. *Nephrology Dialysis Transplantation* **35**, 937–945 (1st June 2020).
11. Jafari, R., Hectors, S. J., González, A. K. K. de, Spincemaille, P., Prince, M. R., Brittenham, G. M. & Wang, Y. Integrated Quantitative Susceptibility and R2\* Mapping for Evaluation of Liver Fibrosis: An Ex Vivo Feasibility Study. *NMR in Biomedicine* **34**, e4412 (2021).
12. Sabouri, S., Fazli, L., Chang, S. D., Savdie, R., Jones, E. C., Goldenberg, S. L., Black, P. C. & Kozlowski, P. MR Measurement of Luminal Water in Prostate Gland: Quantitative Correlation between MRI and Histology. *Journal of Magnetic Resonance Imaging* **46**, 861–869 (2017).
13. Dhatt, R. *et al.* MRI of the Prostate With and Without Endorectal Coil at 3 T: Correlation With Whole-Mount Histopathologic Gleason Score. *American Journal of Roentgenology* **215**, 133–141 (11th Mar. 2020).
14. Uribe, C. F., Jones, E. C., Chang, S. D., Goldenberg, S. L., Reinsberg, S. A. & Kozlowski, P. In Vivo 3 T and Ex Vivo 7 T Diffusion Tensor Imaging of Prostate Cancer: Correlation with Histology. *Magnetic Resonance Imaging* **33**, 577–583 (1st June 2015).
15. Lazari, A. & Lipp, I. Can MRI Measure Myelin? Systematic Review, Qualitative Assessment, and Meta-Analysis of Studies Validating Microstructural Imaging with Myelin Histology. *NeuroImage* **230**, 117744 (15th Apr. 2021).
16. Peters, J. M. *et al.* White Matter Mean Diffusivity Correlates with Myelination in Tuberous Sclerosis Complex. *Annals of Clinical and Translational Neurology* **6**, 1178–1190 (2019).

## 6.8. References

---

17. Moll, N. M. *et al.* Multiple Sclerosis Normal-Appearing White Matter: Pathology–Imaging Correlations. *Annals of Neurology* **70**, 764–773 (2011).
18. Howard, A. F., Mollink, J., Kleinnijenhuis, M., Pallebage-Gamarallage, M., Bastiani, M., Cottaar, M., Miller, K. L. & Jbabdi, S. Joint Modelling of Diffusion MRI and Microscopy. *NeuroImage* **201**, 116014 (1st Nov. 2019).
19. Mollink, J. *et al.* White Matter Changes in the Perforant Path Area in Patients with Amyotrophic Lateral Sclerosis. *Neuropathology and Applied Neurobiology* **45**, 570–585 (2019).
20. Mottershead, J. P. *et al.* High Field MRI Correlates of Myelincontent and Axonal Density in Multiple Sclerosis. *Journal of Neurology* **250**, 1293–1301 (1st Nov. 2008).
21. Seewann, A. *et al.* Diffusely Abnormal White Matter in Chronic Multiple Sclerosis: Imaging and Histopathologic Analysis. *Archives of Neurology* **66**, 601–609 (1st May 2009).
22. Hametner, S. *et al.* The Influence of Brain Iron and Myelin on Magnetic Susceptibility and Effective Transverse Relaxation - A Biochemical and Histological Validation Study. *NeuroImage* **179**, 117–133 (1st Oct. 2018).
23. Stüber, C. *et al.* Myelin and Iron Concentration in the Human Brain: A Quantitative Study of MRI Contrast. *NeuroImage* **93**, 95–106 (1st June 2014).
24. Bagnato, F. *et al.* Untangling the R2\* Contrast in Multiple Sclerosis: A Combined MRI-Histology Study at 7.0 Tesla. *PLOS ONE* **13**, e0193839 (21st Mar. 2018).
25. Reeves, C. *et al.* Combined Ex Vivo 9.4T MRI and Quantitative Histopathological Study in Normal and Pathological Neocortical Resections in Focal Epilepsy. *Brain Pathology* **26**, 319–333 (2016).
26. Huszar, I. N. *et al.* Tensor Image Registration Library: Automated Non-Linear Registration of Sparsely Sampled Histological Specimens to Post-Mortem MRI of the Whole Human Brain. *bioRxiv*, 849570 (26th Nov. 2019).

## 6.8. References

---

27. Huszar, I. N. *et al.* Automated Slice-to-Volume Registration between Histology and Whole-Brain Post-Mortem MRI in *Proc. Intl. Soc. Mag. Reson. Med.* 27 International Society of Magnetic Resonance in Medicine Annual Meeting (Montreal, 16th May 2019).
28. Szumowski, J., Durkan, M. G., Foss, E. W., Brown, D. S., Schwarz, E. & Crawford, D. C. Signal Polarity Restoration in a 3D Inversion Recovery Sequence Used with Delayed Gadolinium-Enhanced Magnetic Resonance Imaging of Cartilage (dGEMRIC). *Journal of Magnetic Resonance Imaging* **36**, 1248–1255 (1st Nov. 2012).
29. Branch, M., Coleman, T. & Li, Y. A Subspace, Interior, and Conjugate Gradient Method for Large-Scale Bound-Constrained Minimization Problems. *SIAM Journal on Scientific Computing* **21**, 1–23 (1st Jan. 1999).
30. Bjarnason, T. A. & Mitchell, J. R. AnalyzeNNLS: Magnetic Resonance Multiexponential Decay Image Analysis. *Journal of Magnetic Resonance* **206**, 200–204 (1st Oct. 2010).
31. Andersson, J. L. R., Skare, S. & Ashburner, J. How to Correct Susceptibility Distortions in Spin-Echo Echo-Planar Images: Application to Diffusion Tensor Imaging. *NeuroImage* **20**, 870–888 (1st Oct. 2003).
32. Le Bihan, D., Breton, E., Lallemand, D., Aubin, M. L., Vignaud, J. & Laval-Jeantet, M. Separation of Diffusion and Perfusion in Intravoxel Incoherent Motion MR Imaging. *Radiology* **168**, 497–505 (1st Aug. 1988).
33. Andersson, J. L. R. & Sotiroopoulos, S. N. An Integrated Approach to Correction for Off-Resonance Effects and Subject Movement in Diffusion MR Imaging. *NeuroImage* **125**, 1063–1078 (15th Jan. 2016).
34. Andersson, J. L. R. & Sotiroopoulos, S. N. Non-Parametric Representation and Prediction of Single- and Multi-Shell Diffusion-Weighted MRI Data Using Gaussian Processes. *NeuroImage* **122**, 166–176 (15th Nov. 2015).
35. Garyfallidis, E., Brett, M., Amirbekian, B., Rokem, A., Van Der Walt, S., Descoteaux, M. & Nimmo-Smith, I. Dipy, a Library for the Analysis

## 6.8. References

---

- of Diffusion MRI Data. *Frontiers in Neuroinformatics* **8**, doi:10 . 3389 / fninf.2014.00008 (2014).
36. Wang, R., Benner, T., Sorensen, A. G. & Wedeen, V. J. *Diffusion Toolkit: A Software Package for Diffusion Imaging Data Processing and Tractography* in *Proc. Intl. Soc. Mag. Reson. Med.* 15 International Society of Magnetic Resonance in Medicine Annual Meeting (Aug. 2007), 3720.
  37. Descoteaux, M., Angelino, E., Fitzgibbons, S. & Deriche, R. Regularized, Fast, and Robust Analytical Q-Ball Imaging. *Magnetic Resonance in Medicine* **58**, 497–510 (2007).
  38. Hess, C. P., Mukherjee, P., Han, E. T., Xu, D. & Vigneron, D. B. Q-Ball Reconstruction of Multimodal Fiber Orientations Using the Spherical Harmonic Basis. *Magnetic Resonance in Medicine* **56**, 104–117 (2006).
  39. Tournier, J. .-.D., Calamante, F., Gadian, D. G. & Connelly, A. Direct Estimation of the Fiber Orientation Density Function from Diffusion-Weighted MRI Data Using Spherical Deconvolution. *NeuroImage* **23**, 1176–1185 (1st Nov. 2004).
  40. Tournier, J.-D., Calamante, F. & Connelly, A. Robust Determination of the Fibre Orientation Distribution in Diffusion MRI: Non-Negativity Constrained Super-Resolved Spherical Deconvolution. *NeuroImage* **35**, 1459–1472 (1st May 2007).
  41. Tax, C. M. W., Jeurissen, B., Vos, S. B., Viergever, M. A. & Leemans, A. Recursive Calibration of the Fiber Response Function for Spherical Deconvolution of Diffusion MRI Data. *NeuroImage* **86**, 67–80 (1st Feb. 2014).
  42. Garyfallidis, E. *Towards an Accurate Brain Tractography* Ph.D. (University of Cambridge, 2013).
  43. Gürses, B., Kılıçkesmez, O., Taşdelen, N., Firat, Z. & Gürmen, N. Diffusion Tensor Imaging of the Kidney at 3 Tesla MRI: Normative Values and Repeatability of Measurements in Healthy Volunteers. *Diagnostic and Interventional Radiology (Ankara, Turkey)* **17**, 317–322 (Dec. 2011).
  44. Jaimes, C., Darge, K., Khrichenko, D., Carson, R. H. & Berman, J. I. Diffusion Tensor Imaging and Tractography of the Kidney in Children:

## 6.8. References

---

- Feasibility and Preliminary Experience. *Pediatric Radiology* **44**, 30–41 (1st Jan. 2014).
45. Notohamiprodjo, M., Dietrich, O., Horger, W., Horng, A., Helck, A. D., Herrmann, K. A., Reiser, M. F. & Glaser, C. Diffusion Tensor Imaging (DTI) of the Kidney at 3 Tesla—Feasibility, Protocol Evaluation and Comparison to 1.5 Tesla. *Investigative Radiology* **45**, 245 (May 2010).
46. Thavarajah, R., Mudimbaimannar, V. K., Elizabeth, J., Rao, U. K. & Ranganathan, K. Chemical and Physical Basics of Routine Formaldehyde Fixation. *Journal of Oral and Maxillofacial Pathology : JOMFP* **16**, 400–405 (2012).